Title

Nonequilibrium design strategies for functional colloidal assemblies.

Journal

Proceedings of the National Academy of Sciences of the United States of America, 120(40)

Authors

Das, Avishek

Limmer, David

Publication Date

2023-10-03

DOI

10.1073/pnas.2217242120

PNAS RESEARCH ARTICLE | CHEMISTRY

Nonequilibrium design strategies for functional colloidal assemblies

Avishek Das[a] and David T. Limmer[a,b,c,d,1]

Edited by Michael P. Brenner, Harvard University, Cambridge, MA; received October 8, 2022; accepted August 17, 2023, by Editorial Board Member Catherine J. Murphy

We use a nonequilibrium variational principle to optimize the steady-state, shear-induced interconversion of self-assembled nanoclusters of DNA-coated colloids. Employing this principle within a stochastic optimization algorithm allows us to identify design strategies for functional materials. We find that far-from-equilibrium shear flow can significantly enhance the flux between specific colloidal states by decoupling trade-offs between stability and reactivity required by systems in equilibrium. For isolated nanoclusters, we find nonequilibrium strategies for amplifying transition rates by coupling a given reaction coordinate to the background shear flow. We also find that shear flow can be made to selectively break detailed balance and maximize probability currents by coupling orientational degrees of freedom to conformational transitions. For a microphase consisting of many nanoclusters, we study the flux of colloids hopping between clusters. We find that a shear flow can amplify the flux without a proportional compromise on the microphase structure. This approach provides a general means of uncovering design principles for nanoscale, autonomous, functional materials driven far from equilibrium.

self-assembly | molecular machines | nonequilibrium

Significance

The synthesis of most functional materials and the operation of all biological systems occurs through self-organization of small components, driven out of thermal equilibrium. Yet, our understanding of the governing principles of efficient self-assembly has been mostly limited to equilibrium systems, where detailed balance simplifies theoretical analysis but introduces strict trade-offs between the structure and dynamics that can be designed. We study and design the autonomous dynamics of self-assembling colloids forming nanoclusters in a steady shear flow. Using computer simulations, we delineate distinct nonequilibrium strategies to break equilibrium constraints and enhance the material function.

Self-assembly is a dynamic process and its optimal design involves simultaneously stabilizing a target structure while preserving a high rate of conversion into it from a fixed set of precursors (1–4). In and near thermal equilibrium, fundamental trade-offs exist between these two design criteria making them difficult to fulfill concurrently (5). For example, strong, specific interactions are needed to stabilize select structures over others, but strong interactions result in the slow relaxation of defects, and highly specific interactions can stifle growth (6). It is known that far-from-equilibrium conditions may generally accelerate rare reactive events (7, 8), and this has been leveraged in simple models of self-assembly (9, 10). However, the extent to which nonequilibrium conditions can aid the design of self-assembling systems by breaking constraints between the factors that stabilize structures and those that aid in the dynamics of their formation is largely unknown. Moreover, there is currently a lack of general principles to inform strategies employing nonequilibrium conditions to assemble materials with unique structure or function, beyond what is possible in equilibrium. Specific examples in colloidal systems however point to the potential utility of such strategies (11–13). Here, we present a framework for learning the optimal design principles for a general nonequilibrium self-assembling system, and demonstrate how the continuous injection of energy significantly expands the available design space of functional materials assembly.

Functional materials cycle between multiple conformations in order to achieve a dynamical task. Any functional structure like an enzyme or a molecular motor must not only be stable but also necessarily able to disassemble and reassemble in a dynamic nonequilibrium steady-state (14, 15). Such materials typically form internal reaction networks of disassembled intermediates with multiple nonzero reactive fluxes, driven by external forces that are autonomous (16–19). Autonomous driving is time-independent, energetically cheap to implement, and acts nonspecifically on the entire system (20). Functional materials efficiently transduce chemical and mechanical energy by optimally coupling the external dissipative forces to specific edges in their internal reaction networks. This may modify reactive fluxes and break detailed balance in those reaction coordinates that are then coupled to their output work. Thus, optimizing the dynamics of self-assembly for probability fluxes in and out of a target structure is the path to designing functional materials. However, a framework for doing so is complicated as typical relationships concerning stability and response valid in equilibrium no longer hold.

Using a nonequilibrium variational framework, we develop a route to identify design rules for driven self-assembly. This framework uses insights from large deviation theory

Author affiliations: [a]Department of Chemistry, University of California, Berkeley, CA 94720; [b]Chemical Sciences Division, Lawrence Berkeley National Laboratory, Berkeley, CA 94720; [c]Material Sciences Division, Lawrence Berkeley National Laboratory, Berkeley, CA 94720; and [d]Kavli Energy NanoSciences Institute, University of California, Berkeley, CA 94720

Author contributions: A.D. and D.T.L. designed research; A.D. and D.T.L. performed research; A.D. analyzed data; and A.D. and D.T.L. wrote the paper.

The authors declare no competing interest.

This article is a PNAS Direct Submission. M.P.B. is a guest editor invited by the Editorial Board.

[1]To whom correspondence may be addressed. Email: dlimmer@berkeley.edu.

This article contains supporting information online at https://www.pnas.org/lookup/suppl/doi:10.1073/pnas.2217242120/-/DCSupplemental.

Published September 25, 2023.

and stochastic thermodynamics (21, 22). In particular, we probe the dynamics and outcome of self-assembly by analyzing order parameters over trajectories from molecular dynamics simulations (23–25). Previous work on optimizing the reactivity of self-assembled colloidal clusters have used Kramers approximations valid only at equilibrium (26) or have looked at single transient realizations of reactive barrier crossing (27). The design of optimal disassembly and reassembly, i.e., nonzero probability fluxes and currents in and out of functional structures in nonequilibrium steady-states, remains unexplored. Employing a variational principle, we adapt a previous algorithm used to study the optimal design of passive DNA-coated colloids, to design instead for enhanced reactive fluxes. We study the effectiveness of this approach in isolated colloidal nanoclusters and in a microphase of many nanoclusters, both in a sheared nonequilibrium steady-state. Using the inverse design algorithm and rationalizing the discovered designs in parameter space, we find nonequilibrium strategies for breaking trade-offs between structure and dynamics.

Model of DNA-Coated Colloids

We have modeled the self-assembly of DNA-labeled colloidal nanoparticles via overdamped Langevin dynamics simulations of N particles, interacting pairwise with a coarse-grained potential $V(r)$, with r being the center-to-center distance between two colloids, Fig. 1*A*. The potential consists of a volume-exclusion repulsion modeled with a Weeks-Chandler-Andersen (WCA) potential (28) with an exclusion diameter of σ, and selective short-range attractive interactions modeled with a Morse potential with amplitude D_{ij} between pairwise particle indices i and j. Such a potential has been demonstrated previously to accurately represent selective attractions between two DNA-labeled surfaces (29, 30). Self-assembly with this model can be designed to yield nanoclusters of prespecified sizes and symmetry, by tuning D_{ij} with respect to $k_{\mathrm{B}}T$, or Boltzmann's constant times temperature (21, 31, 32). We consider this self-assembling system evolving within a nonequilibrium steady-state under a shear flow with a constant shear flow rate f. The shear flow displaces the particles by competing with the natural diffusive velocity gradient scale for the system, $f^* = k_{\mathrm{B}}T/\sigma^2$. Given the mechanical driving force of shear performs dissipative work on the system, it may change the relative stability of configurations as well as the rate of interconversions between them. We investigate whether optimal design principles can be found that can tune the dynamics of self-assembly independently from configurational probabilities for prespecified target order parameters.

Equilibrium Constraints on Self-Assembly Dynamics

Thermal equilibrium constrains the dynamics of rates of interconversion between stable self-assembled structures to the yields of those structures. Both quantities can be viewed as trajectory-averaged quantities. We denote a simulated trajectory of particle positions $\mathbf{r}^N(t)$ as a function of time t, by $X = \{\mathbf{r}^N(0), \mathbf{r}^N(\delta t), \ldots, \mathbf{r}^N(t_f)\}$, with t_f being the duration of the trajectory and δt the simulation time step. We take t_f much longer than the free colloidal diffusion timescale $t^* = \gamma\sigma^2/k_{\mathrm{B}}T$, where γ is the friction coefficient for the free colloids in solution, such that the colloids relax into a steady-state and trajectory averages of order parameters are independent of t_f. The expected yield, Y_{A}, of any target structure A over this trajectory can be computed from a trajectory average of the indicator function,

$$Y_{\mathrm{A}} = \frac{1}{t_f}\int_0^{t_f} \mathbf{1}_{\mathrm{A}}[\mathbf{r}^N(t)]dt, \qquad [1]$$

where $\mathbf{1}_{\mathrm{A}}[\mathbf{r}^N(t)]$ returns 1 when the system is in state A and is 0 otherwise. For computing the interconversion rates, we first define the probability flux from state A to state B, q_{AB}. The steady-state flux can be evaluated from a two-time correlation function between the indicator functions for state A and B over a lag-time τ,

$$q_{\mathrm{AB}} = \frac{1}{\tau(t_f-\tau)}\int_{\tau}^{t_f} \mathbf{1}_{\mathrm{A}}[\mathbf{r}^N(t-\tau)]\mathbf{1}_{\mathrm{B}}[\mathbf{r}^N(t)]dt, \qquad [2]$$

which is a time-scaled, joint probability of being in A at some time and being in B after time τ. This flux directly counts the number of times A transfers to B over a trajectory. If the lag-time τ is larger than the relaxation time within the A state, but much smaller than the typical waiting time for the transition, q_{AB} reports on the rate constant k_{AB} as $k_{\mathrm{AB}} = q_{\mathrm{AB}}/Y_{\mathrm{A}}$, independent of τ (33).

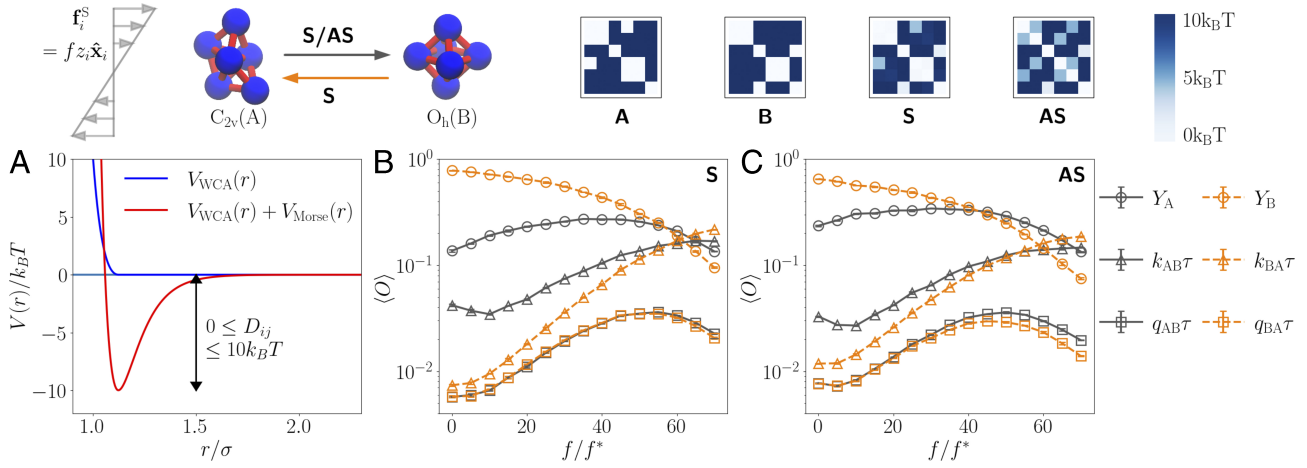

Fig. 1. Optimal probability flux between polytetrahedron and octahedron. (*Top panel*) Schematic of isomerization reaction. Volume exclusion due to the colloids is shown in blue, and tunable pairwise bonds are shown in red. Optimal *alphabets* for high yield and high flux. (*A*) Pairwise interaction potential. (*B*) and (*C*) Average values of observable $\langle O\rangle \in \{Y, k\tau, q\tau\}$ with respect to shear, keeping the alphabets fixed at **S** and **AS**.

In thermal equilibrium, probability fluxes are balanced, such that $q_{AB} = q_{BA}$ and the probability current $j_{AB} \equiv q_{AB} - q_{BA} = 0$. This implies that the ratio of forward and backward rates of interconversion k_{AB} and k_{BA} is strictly coupled to the relative stability of A and B, $k_{AB}/k_{BA} = Y_B/Y_A$. A configuration that is more energetically stable is necessarily less reactive at equilibrium, and thus the rate of error correction and annealing toward the globally stable state is reduced. This trade-off is the reason for the existence of an optimal zone for self-assembly in or near thermal equilibrium (5). Far-from-equilibrium conditions may be designed to stabilize otherwise unstable or exotic structures, but may not always break detailed balance, if the driving force does not couple to the relevant reactive mode. We describe next how to design far-from-equilibrium steady-states to tune rate constants and structural stabilities independently, and how to break detailed balance in any target coordinate.

Optimal Design of Function

We use an iterative optimization algorithm to find the best choice of design parameters $\{D_{ij}\}$ and shear flow rate f that maximizes fluxes q_{AB} or currents j_{AB} for a given choice of states A and B. We construct a cost function for optimization, $\langle\Omega\rangle$, that encodes the minimal change to a reference system to maximize either observable by minimizing the Kullback–Leibler divergence between the steady-states of the reference and the controlled system (21). For the overdamped dynamics we consider, this is given by $\langle\Omega\rangle = \left\langle \lambda O - \sum_{i=1}^{N} (\mathbf{u}_i - \mathbf{F}_i)^2 / 4\gamma k_B T \right\rangle$, where λ is a biasing parameter, O is a time-averaged static or dynamic order parameter, q_{AB} or j_{AB}, for example, $\mathbf{u}_i$ is the total force that the i-th particle experiences, $\mathbf{F}_i$ is the WCA force from the interparticle potential, and $\langle \dots \rangle$ denote an average over the steady-state. The second term, deriving from the Kullback–Leibler divergence between trajectory ensembles with and without the added force $\mathbf{u}_i - \mathbf{F}_i$ (22), acts as a regularizer for the optimization in regions of design space where the first term is either zero or degenerate. We optimize $\langle\Omega\rangle$ through stochastic gradient descent by computing its explicit gradients with respect to any design parameter c, from a generalized fluctuation-response relation

$$\frac{\partial\langle\Omega\rangle}{\partial c} = \left\langle \frac{\partial\Omega}{\partial\mathbf{u}} \cdot \frac{\partial\mathbf{u}}{\partial c} \right\rangle + \int_0^\infty \left\langle \delta\Omega(t)\delta \left(\frac{\partial \dot{\ln} P[X]}{\partial\mathbf{u}} \cdot \frac{\partial\mathbf{u}}{\partial c} \right)(0) \right\rangle dt, \quad [3]$$

where $P[X]$ is the Onsager-Machlup probability of trajectory X (34, 35). We choose initial values for the design parameters such that $\langle O\rangle$ is nonzero, simulate a steady-state molecular dynamics trajectory to converge the terms in Eq. **3**, change the design parameters by taking a gradient descent step, and keep iterating until we converge to a locally optimal design. In practice, we find that as the gradients are stochastic, noise enhances the exploration of parameter space and helps anneal rapidly into the global optimum (21). We nevertheless test the uniqueness of each solution basin by starting the optimization from different points in parameter space, such as from high-yield designs for A and B, or from a nonspecific attraction that results in moderate yields of both. During optimization, we constrain the magnitude of the bond energies to stay less than $10k_BT$ so that there are no long-lived kinetic traps that prevent the relaxation of the system into a steady-state (36). In case of a breakdown in ergodicity, the steady-state gradient expression in Eq. **3** would not be accurate, instead the gradients of probability of finite duration trajectories would need to be used (8). Further details about the variational algorithm and a pseudocode are in *SI Appendix*.

Symmetric and Asymmetric Strategies for Maximal Flux. We first apply this algorithm to the interconversion between polytetrahedral (A: C_{2v}) and octahedral (B: O_h) configurations in a sheared steady-state with $N = 6$ particles, for a fixed choice of lag-time $\tau = 0.025t^*$, slightly longer than typical transition timescales. The optimal design that maximizes yields Y_A and Y_B are known to be the Maximal Alphabet **A** and **B** for the D_{ij} matrix, shown schematically in Fig. 1, in which a uniform attractive energy stabilizes each contact pair (21, 36). Alphabet matrices possess a degeneracy to permutations of particle indices, a symmetry that the variational optimization spontaneously breaks (21). In order to interpret physically meaningful distinctions between alphabets and to interpolate between them, we have permuted them to be the least different (see *SI Appendix* for details).

Optimization for maximal q_{AB} yields $f/f^* = 50$, the highest allowed value during optimization, and two distinct D_{ij} alphabet solutions, denoted **S** and **AS**. Maximizing q_{BA} however yields only the alphabets **S**. Fig. 1*B* shows a slice through the design space in the direction of varying f but keeping D_{ij} fixed. Far-from-equilibrium conditions amplify the fluxes by increasing the rates of interconversion in both directions. At $f = 0$, detailed balance constraints $q_{AB} = q_{BA}$ as seen by the trade-offs in (Y_A, k_{AB}) and (Y_B, k_{BA}). The **S** matrix maximizes both q_{AB} and q_{BA} symmetrically, such that probability flows predominately between states A and B even far-from-equilibrium. This is accomplished with alphabet **S** being intermediate in bond-strength to the alphabets **A** and **B**. **S** preserves the common bonds in **A** and **B** and codes for weak bond energies for the unique bond in each structure.

With the other solution **AS**, shear flow amplifies the flux in the forward direction more than the reverse, breaking detailed balance. Fig. 1*C* shows how this is achieved by starting with a Y_A higher than the previous case and thus a smaller k_{AB}, at equilibrium. At high shear, k_{AB} is amplified to similar absolute values as with **S**, without a proportional reduction in Y_A. The solution **AS** codes for a dynamical bonding arrangement different from **A** or **B**. This class of asymmetric high-flux solutions is generally found as a locally optimal design for other pairs of nanoclusters as well. We note that the alphabet in question is not asymmetric, as it is generated from pairwise conservative interactions, but rather that the alphabet causes q_{AB} and q_{BA} to be asymmetrically amplified, breaking detailed balance.

In both cases, the fluxes reach a maximum with f before turning over and decaying at large shear rates that are nevertheless experimentally achievable in microfluidic devices (37). This turnover arises from a competition between the enhancement of diffusive exploration of the internal degrees of freedom till moderate flow rates, and the destabilization of bonds at high flow rates. This turnover is similar in origin to a turnover previously reported in shear-induced crystallization rates of hard spheres at high supersaturation, where the cohesive free energy is much larger than k_BT (38).

Strategy for Maximal Probability Current. For the same polytetrahedron (A) and octahedron (B) clusters, we have also found the optimal D_{ij} matrices and shear flow rates f that maximize the probability currents j_{AB} and j_{BA}. For j_{AB}, we find the optimal solution to be f/f^* close to 50 and alphabet **C**, shown in Fig. 2. For j_{BA} optimization, we do not find any design where j_{BA} is positive. The optimization algorithm always finds the trivial maximum with low D_{ij} where $Y_A = Y_B = 0$. A slice through the parameter space in the f direction, keeping alphabet **C** fixed, is

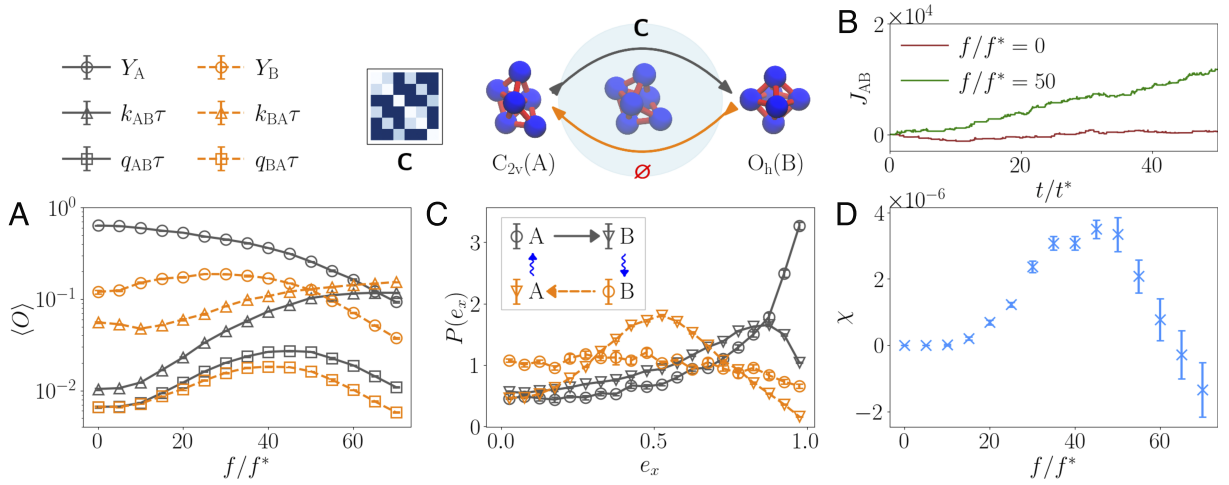

Fig. 2. Optimal breakdown of detailed balance induced by shear flow. (*Top left and center*) Optimized alphabet for high current. Schematic of the isomerization intermediate. (*A*) Reactive displacement trajectories $J_{AB}(t)$. (*B*) Average values of observable $\langle O \rangle \in \{Y, k\tau, q\tau\}$ with respect to shear, keeping the alphabet fixed at **C**. (*C*) Probability distribution of the orientation of the nanocluster, e_x, while in steady-state in A (black circles), immediately after an A → B reaction (black triangles), steady-state in B (orange circles), and immediately after a B → A reaction (orange triangles). Blue arrows in the inset denote orientational relaxation. (*D*) Difference of covariance of shear work W and the time spent in 11-bonded state τ_I, during forward and backward transitions.

shown in Fig. 2*A*. The algorithm has found a design to break detailed balance maximally in this prespecified direction, by decoupling constraints between (Y_A, k_{AB}) and (Y_B, k_{BA}). When we compare these observables to those with the symmetric high-flux alphabet **S** in Fig. 1*B*, we find that the high current with **C** arises due to Y_B having a quicker turnover than before. An equivalent explanation is k_{BA} does not increase as expected from detailed balance considerations. As a result, structural constraints have been decoupled optimally from rate constraints in nonequilibrium. The gap between Y_A and Y_B in log-scale, exactly balanced at equilibrium by the gap between k_{AB} and k_{BA}, has been designed to no longer be so at the optimal shear.

Broken detailed balance results in a reactive displacement over time $J_{AB}(t) = \int_{\tau}^{t+\tau} \left[\mathbf{1}_A(t'-\tau)\mathbf{1}_B(t') - \mathbf{1}_B(t'-\tau)\mathbf{1}_A(t')\right]dt'$, where the full arguments of the indicators have been suppressed for brevity. The expectation of this observable counts the difference between the expected number of transitions happening in the forward and backward directions. In Fig. 2*B*, we have shown a typical trajectory of the reactive displacement with time, at zero and optimal shear rate, for the alphabet **C**. The approximately uniform and rapid growth of J_{AB} with time, and the comparable magnitudes of fluctuations in the two curves, shows how the shear is preferentially amplifying the reactive flux in the forward direction and that this happens through a higher number of small jumps rather than through large rare events. This suggests that the reactive cycle involved in breaking detailed balance in the A → B coordinate consists of all edges with comparable reaction rates and comparable changes in configuration space.

Shear flow is a nonspecific mechanical force acting on all particles, yet it is able to drive a reactive cycle in the internal coordinates of the nanocluster. This is achieved through autonomous relaxations in the orientation of the nanoclusters. We demonstrate this by plotting probability distributions of the x-component of the normalized principal eigenvector of the gyration tensor of the nanocluster, e_x, in Fig. 2*C*. The x component of the gyration tensor e_x measures the orientational alignment of the cluster in the flow direction. Aspherical clusters like A have larger typical value of e_x than approximately spherical clusters like B, which does not align in the flow. We find that immediately after reactions in both directions, orientations of the clusters are significantly different from their steady-state values. Orientational motion aided by shear flow and conformational transitions thus form a reactive cycle with a nonzero current.

The distinction between the forward and backward transition paths with alphabet **C** in the presence of shear flow can be quantified mechanistically. Both clusters have 12 bonds, but to transition between the two states requires breaking a bond on the concave face of the C_{2v} structure, passing through an 11-bonded intermediate as shown in Fig. 2, and then rebonding of two different particles on that face. The optimized alphabet **C** stabilizes this motion by weakening the bond in A located directly opposite to its concave face. We have computed the effect of shear flow on the transition paths through the covariance between the time spent in the 11-bonded intermediate, τ_I, and the work done by shear flow, $W = \sum_{i=1}^{N} \int_{t_1}^{t_2} \mathbf{f}_i^S(\mathbf{r}_i).\dot{\mathbf{r}}_i dt$, which is integrated between t_1 and t_2, the start and end of forward and backward transition paths. The difference in covariance $\chi = \langle \delta\tau_I \delta W \rangle_{AB} - \langle \delta\tau_I \delta W \rangle_{BA}$, between forward and reverse reaction paths, is plotted in Fig. 2*D*, with respect to increasing shear. The difference in the covariance increases initially and then peaks near the optimal shear flow for high current. This implies that even at the level of individual trajectories, spending time in the 11-bonded intermediate state is correlated with the effect of shear more in the trajectory ensemble of forward reactions than the reverse ones. Past the turnover, the difference becomes smaller and then negative, with fluctuations that grow with further increasing shear, suggesting participation of competing sheared reaction pathways involving more broken bonds.

Detailed studies of the local stability of these strategies in design space (*SI Appendix*) show that detailed balance is preserved all along linear interpolations in parameter space between **A** → **S** → **B** even in a high shear flow, with the highest flux occurring at **S** as found by the optimization algorithm. Employing similar interpolations between **S** → **AS** → **C**, we find that q_{AB} increases monotonically between **C** → **AS**, which explains why **AS** can be identified by gradient descent when starting from **C**. The close connection between solutions **C** and **AS** suggests that the existence of a nontrivial high current locally optimal solution in

any reaction direction depends on the existence of an asymmetric high flux solution with a positive current.

Generality of Nonequilibrium Strategies

We can better understand the coupling between shear-driven orientation and the conformational change through a minimal model of a colloidal dimer in shear flow $\mathbf{f}_i^{\mathbf{S}} = fz_i\mathbf{x}_i$ constrained to the $x-z$ plane for simplicity. We assume that the dimer isomerizes between two states α_1 and α_2, with center-to-center distances L_1 and L_2, respectively, and equilibrium rates $k_{12} = k_0$ and $k_{21} = k_0 e^{\beta\Delta V}$, where ΔV is the potential energy difference between α_2 and α_1. This is schematically illustrated in Fig. 3*A*. We assume $L_2 = L_1 + \Delta L$, such that a shear flow may stretch the dimer and increase the rate of isomerizing from α_1 to α_2. We assume the reactions occur at fixed orientation, and in between reactions, the orientation of the dimer relaxes in the shear flow. The orientation is quantified by the angle $\theta \in (0, 2\pi)$ where $\cos\theta \equiv \hat{\mathbf{e}} \cdot \hat{\mathbf{x}}$ with $\hat{\mathbf{e}}$ being the dimer axis. The torque due to the shear flow depends on the state $\alpha_{j\in(1,2)}$ and is given by $\Gamma = fL_j^2[1-\cos(2\theta)]/4$, which together with an angular diffusion constant D_θ, relaxes the distribution $P(\theta)$. In the limit of small fL_j^2/D_θ, the distribution $P_j(\theta)$ for each state $\alpha_{j\in(1,2)}$ can be computed as a perturbation over free diffusion, $P_j(\theta) = \{1 + [8D_\theta p \sin 2\theta - p^2(\cos 4\theta - 4\cos 2\theta)]/16D_\theta^2\}N_j/2\pi$, where $p = fL_j^2/4$ and N_j is a normalization factor (39). Longer clusters thus align more with shear flow, similar to Fig. 2*C*. We further assume that the yields of α_1 and α_2 do not change from equilibrium, such that $N_1/N_2 = e^{\beta\Delta V}$, consistent with our explicit model findings.

Given an orientation, the stretching force is $\Pi = fL_j \sin(2\theta)/4$ and up to linear order in ΔL, the rates of extension and compression are affected as $k_{12} = k_0 e^{\beta\Pi\Delta L\cos\phi_1}$ and $k_{21} = k_0 e^{\beta(\Delta V + \Pi\Delta L\cos\phi_2)}$, respectively (7), where $\phi_{j\in(1,2)}$ is the angle between the reaction coordinate and the stretching mode. We can now compute the forward and backward fluxes as probability times reaction rate integrated over all θ. The steady-state reactive current from α_1 to α_2 becomes

$$j_{12} = \frac{k_0 L^3}{64 D_\theta^2 [1 + e^{-\beta\Delta V}]} \Delta L(\cos\phi_1 - \cos\phi_2) f^2, \qquad [4]$$

in the limit of small $\Delta L/L$ where $L = (L_1 + L_2)/2$. The quadratic response of the current in the limit of small ϕ_j is illustrated in Fig. 3*B*. Hence, shear flow is able to produce a reactive current by coupling internal conformation with global orientation in a four-stroke cycle, with the sign of the current depending only on the geometry of the reaction coordinates. While simple, this model explains the observed features in the self-assembly of nanoclusters, such as why there exist no solutions for positive current in some reaction directions. Based on our minimal model, bidirectional currents are only possible when there exist multiple reaction mechanisms, i.e., different sets of (ϕ_1, ϕ_2). Further, the dimer model predicts that the magnitude of the current j_{12} increases with increasing ΔV, i.e., with a more stable α_1, when the timescale arising from k_0 is held constant. This rationalizes the observation that the alphabet **C** in Fig. 2*A* that drives current j_{AB} has a higher Y_A/Y_B at equilibrium, compared to alphabet **S**.

A high reactive flux simultaneously in both directions is achieved through having a low free-energy barrier such that the reaction timescale is faster than shear-induced rotations, with the fluxes being amplified symmetrically by a shear flow. A high reactive current is achieved through having a favorable reaction coordinate geometry and an intermediate barrier height, to slow down the reactive timescale and couple it to rotational timescale. For nanocluster rearrangements where the free energy barrier and reaction coordinate geometry are not available, the variational algorithm can directly optimize for the reactive flux and current. We note that this method of converting mechanical driving to chemical work through switchable geometry is reminiscent of the blood-clotting protein von Willebrand factor that uses the shear flow to unfold (40). The shear-induced enhancement of reactive flux and current in our theory is contingent only on two aspects, the alignment of aspherical clusters along a shear flow, and the modulation of reaction rates by dissipative driving. Both are general results with numerical and experimental verification in colloidal suspensions (7, 41, 42), polymers (43, 44), and biomolecules (45, 46).

The generality of the principle can be tested by studying probability fluxes and currents for interconversions between four rigid nanoclusters with $N = 7$ DNA-labeled particles, as shown in Fig. 3 *C* and *D*, with additional results in *SI Appendix*. These are the four highest yield clusters at equilibrium for a nonspecific short-range pairwise attraction (21, 36). We find that the nonequilibrium strategies discovered for interconverting the polytetrahedron and octahedron nanoclusters are also applicable more widely. When pairwise interaction matrices are set to the optimized alphabets, most reactive fluxes are amplified by a far-from-equilibrium shear flow due to a larger enhancement in rate constants compared to the decay in yields. The far-from-equilibrium optima exhibit qualitatively different dynamics than a near-equilibrium perturbative regime. For high probability flux in pairwise transitions, in most cases, we find locally optimal symmetric alphabets that preserve detailed balance even far-from-equilibrium. The symmetric solutions are always locally optimal in both forward and reverse directions of the transitions. As before, these solutions result from restricting

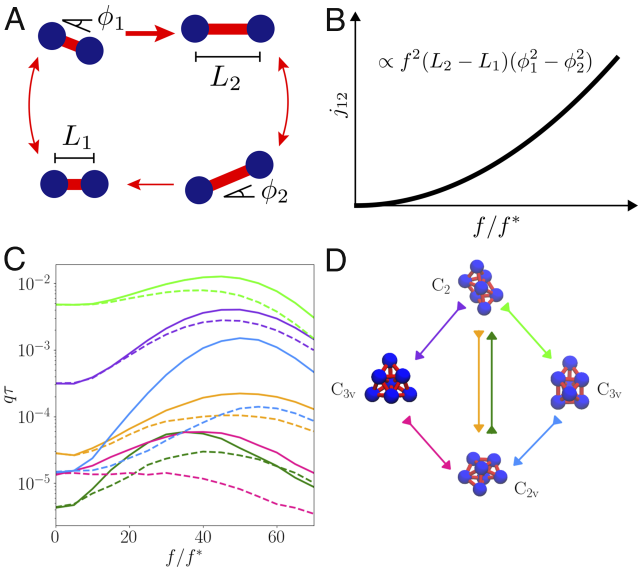

Fig. 3. Design for maximal probability current. (*Top* row) Minimal model of the shear-induced reactive cycle for a two-dimensional colloidal dimer. (*A*) Reactive cycle comprising of shear-dependent reactions followed by shear-dependent orientational relaxations. (*B*) Quadratic response of the probability current to an increasing shear flow. (*C*) Profile of reactive currents in 7-particle clusters with changing shear, keeping the optimized alphabets fixed. Solid (dashed) lines represent forward (backward) reactive flux. Colors correspond to the specific edges in the reaction network in (*D*).

transitions between only these two tagged configurations, and preventing leakage to competing structures. In many cases, we find distinct locally optimal asymmetric alphabets that break detailed balance at large f. The alphabets for this strategy are typically only optimal for reactive flux in one reaction direction. When optimized for high probability current, we find many locally optimal alphabets that channel the shear flow into breaking detailed balance in a particular reaction direction and thus maximize the difference between forward and backward reactive flux. These alphabets are distinct from, but closely related to, the asymmetric high-flux alphabets. For any given reaction, optimal high-current solutions exist if and only if there are optimal asymmetric high-flux solutions that have a positive current.

Particle Hopping Flux in a Sheared Microphase

Extending these strategies to a macroscopic system of DNA-labeled colloids straightforwardly requires a prohibitive $\mathcal{O}(N^2)$ scaling of the necessary alphabet size, as any colloid in a distinct nanocluster must not attract bonding partners from adjacent nanoclusters (32, 36). This attraction is a nanoscale manifestation of surface tension that tries to relax the system toward a bulk condensate. If however a long-range repulsion arising from a screened Coulomb interaction is combined with the short-range DNA-labeled attractive forces, large systems can self-assemble into a microphase at equilibrium, characterized by the spontaneous emergence of an intermediate length-scale at which nanoclusters are stabilized (47, 48). Microphase separation or self-limited assembly is often used in biological systems to regulate the volumes of viral capsids, cells, and membraneless organelle (49–51).

Self-limited clusters in biological systems are not static structures but highly fluxional. Nonequilibrium surface reactions are used by cells to stabilize microphase droplets (52–54), and components of self-limited clusters continuously exchange with the surrounding solute pool in a dynamic steady-state (55). Here, we focus on how to tune the dynamics of particle exchange between nanoclusters given we have a microphase-separated state. By studying the optimal design of a particle hopping flux between multiple nanoclusters, we demonstrate that a sheared nonequilibrium steady-state can break equilibrium constraints relating stability and flux.

We start with a microphase-separated state at equilibrium, self-assembled from DNA-labeled colloids having a pairwise repulsive Yukawa potential $V(r) = \epsilon \exp(-\kappa r)/r$ in addition to the previous short-ranged interactions. We are interested in the yield and reactive flux of compact nanoclusters consisting of 6 colloids and with at least 9 bonds, regardless of its shape. Such nanoclusters are denoted as state A. The cutoff on the number of bonds ensures we are accurately counting reactions involving hopping of particles between clusters instead of complete dissociation of a cluster. We calculate the average yield Y_6, by checking whether each particle is in a cluster of type A, as $Y_6 = \int_0^{t_f} \sum_{i=1}^{N} \mathbf{1}_{i\in\mathrm{A}}(t)dt/Nt_f$. For counting particle hops we take a lag-time $\tau = 0.025t^*$ slightly larger than the timescale of typical adsorption and desorption transitions of colloids from nanoclusters. With this, our hopping flux between 6-colloid clusters becomes

$$q_6 = \frac{1}{N\tau(t_f-\tau)} \int_{\tau}^{t_f} \sum_{i=1}^{N} \mathbf{1}_{i\in\mathrm{A}'}(t-\tau)\mathbf{1}_{i\in\mathrm{A}''}(t)dt, \quad [5]$$

where A′ and A″ refer to distinct clusters of type A with the only common particle being that with index i. This condition ensures that only the exchange of a single particle at a time, i.e., a hop, is being counted, as illustrated in Fig. 4 *A*, *Inset*.

As we are not recording the shapes of clusters so long that they are compact, we do not use an alphabet in our design space,

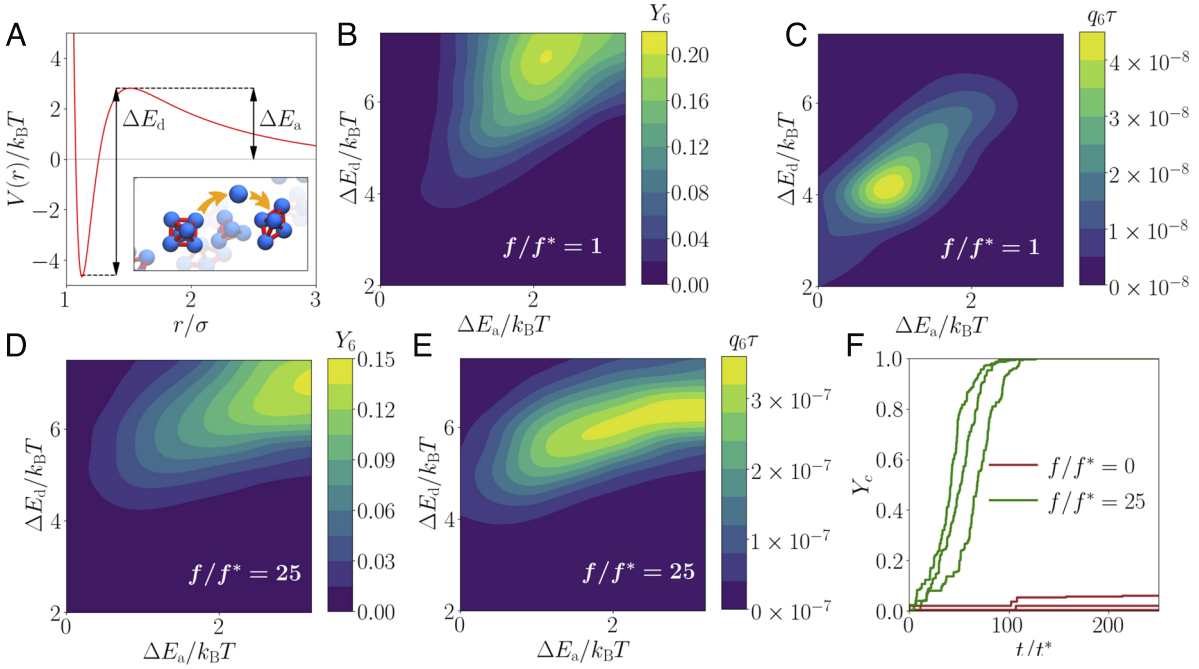

Fig. 4. Independent tuning of hopping flux and microphase structure by shear flow. (*A*) Pairwise interaction potential. (*Inset*) Schematic illustration of hopping in a microphase. (*Center* and *Right* columns) Color maps of (*B*) Y_6 at $f/f^* = 1$, (*C*) $q_6\tau$ at $f/f^* = 1$, (*D*) Y_6 at $f/f^* = 25$ and (*E*) $q_6\tau$ at $f/f^* = 25$, with respect to changing assembly and disassembly barriers. Corresponding color scales are indicated next to each color map. (*F*) Trajectories of the yield of particles of color (*c*) as a function of time, with different noise realizations.

but rather a nonspecific value of the attraction D that competes against the repulsion energy scale ϵ over a length-scale of κ^{-1}. We constrain the total pairwise force and potential to go to zero at a cutoff distance of 5σ with a shifted forces approximation (56). This constraint leaves the potential energy function with two relevant effective features, the energy barrier to bond formation or the assembly barrier ΔE_a, and the energy barrier to bond breaking or the disassembly barrier ΔE_d, shown in Fig. 4*A*. We study the effect of far-from-equilibrium conditions on Y_6 and q_6 by variationally optimizing D, ϵ, and κ, keeping the shear flow rate fixed at $f/f^* = 1$ and 25. We also compute the yield and reactive flux landscape by directly sweeping over the design parameters such that we can elucidate their dependence on ΔE_a and ΔE_d.

Breaking Equilibrium Constraints on Hopping Flux. At equilibrium, large values of both barriers ΔE_d and ΔE_a stabilize the microphase, where their difference $\Delta E_d - \Delta E_a$ is the energy gain on forming a new bond starting from a dispersed state. The reactive flux for the bond formation and breakage, however, is dependent on both of these energy barriers, slowing exponentially as they increase. As can be anticipated from detailed balance, near equilibrium changing ΔE_d or ΔE_a to optimize yield degrades the reactive flux and vice-versa. This trade-off is shown near thermal equilibrium, $f/f^* = 1$, in Fig. 4 *B* and *C* in maps of Y_6 and q_6, for a system of $N = 90$ colloids at a packing fraction $\phi = 0.02$, where the yield and reactive flux both exhibit narrow peaks at distinct parameters.

Far-from-equilibrium, however, the constraint between yield and reactive flux is decoupled, and both have broad regimes of near-optimal behavior that overlap one another. Shear flow thus allows an optimal regime in parameter space having high yield of a microphase as well as a high reactive flux of particles hopping between nanoclusters. This occurs by expanding the regime of stability of the microphase over a broader ΔE_a range than near equilibrium (Fig. 4 *D* and *E*) through stabilizing nonrigid nanoclusters (21). These nonrigid clusters are compact with $\geq$ 9 bonds in total, but have dangling bonds that are energetically more susceptible to break, contributing to a high hopping flux. We find that though far-from-equilibrium shear flow reduces the yield of the nanoclusters by 30% from the near-equilibrium regime, the highest reactive flux is amplified by more than 600%. This points to a large amplification in the underlying rate constants by the breakdown of equilibrium constraints. We also show in *SI Appendix* that the enhancement of hopping flux is explained by the alignment of nonrigid clusters in the shear flow and the enhancement of diffusion constant in the flow direction. These findings are in qualitative agreement with the shear-induced flux enhancement in our dimer model. In all cases the variational algorithm optimizes the parameters accurately to arrive close to the optima given it is started from a point in parameter space where either observable is measurably nonzero (*SI Appendix*).

We have demonstrated an application of the increased hopping flux between nanoclusters by an example of an autocatalytic switching reaction. We assume that colloids in the nanoclusters are energetically identical but each carries a color, c or nc, similar to phosphorylation tags on biomolecules or competing conformations in proteins (55, 57). At $t = 0$ in a steady-state, only one particle is initialized as c with the rest being nc. Every time a c-colored particle is in a cluster of type A, it instantly converts every other particle in the cluster to c, similar to models for cooperative switching in biomolecules (58). The yield Y_c of particles of color c is expected to increase fastest when colloids from type A clusters hop fastest directly to other type A clusters in a steady-state. Keeping D, ϵ, and κ fixed at the optimal value for the highest microphase yield Y_6 at $f/f^* = 1$, we show example trajectories of Y_c for $f/f^* = 0$ and 25 with a system size $N = 300$, in Fig. 4*F*. We find that the far-from-equilibrium system indeed shows a higher rate of increase of Y_c over the equilibrium scenario. At this optimal design, the mechanical and nonspecific shear driving has been optimally channeled into amplifying reactive flux in the hopping reaction coordinate.

We note that the reactive fluxes we discussed are autonomously driven within the sheared steady-state assembly. The design principles we found rely on coupling an external nonspecific driving force to an internal reaction coordinate through an autonomously self-organizing degree of freedom, the geometry. The accompanying algorithm can numerically expose such design rules. Our insights on how such motifs can break equilibrium constraints in specific reaction coordinates can help design molecular machines that efficiently transduce energy through internal rearrangements (20). This work also opens a promising window toward designing dynamical phases of functional materials and shows how to tune fluxionality without compromising structure, by going to nonperturbative far-from-equilibrium regimes (59).

Materials and Methods

A pseudocode of our optimization algorithm, a detailed description of the numerical simulations, learning curves, and optimal alphabets are available in *SI Appendix*.

Data, Materials, and Software Availability. Code data have been deposited in Zenodo (10.5281/zenodo.8031998) (60).

ACKNOWLEDGMENTS. This work has been supported by NSF Grant CHE-1954580. A.D. was also supported by the Philomathia Graduate Student Fellowship from the Kavli Energy Nanoscience Institute at University of California Berkeley.

1. G. M. Whitesides, B. Grzybowski, Self-assembly at all scales. *Science* **295**, 2418–2421 (2002).
2. W. M. Jacobs, A. Reinhardt, D. Frenkel, Rational design of self-assembly pathways for complex multicomponent structures. *Proc. Natl. Acad. Sci. U.S.A.* **112**, 6313–6318 (2015).
3. C. J. Fullerton, R. L. Jack, Optimising self-assembly through time-dependent interactions. *J. Chem. Phys.* **145**, 244505 (2016).
4. I. Coropceanu *et al.*, Self-assembly of nanocrystals into strongly electronically coupled all-inorganic supercrystals. *Science* **375**, 1422–1426 (2022).
5. S. Whitelam, R. L. Jack, The statistical mechanics of dynamic pathways to self-assembly. *Annu. Rev. Phys. Chem.* **66**, 143–163 (2015).
6. S. Whitelam, E. H. Feng, M. F. Hagan, P. L. Geissler, The role of collective motion in examples of coarsening and self-assembly. *Soft Matter* **5**, 1251–1262 (2009).
7. B. Kuznets-Speck, D. T. Limmer, Dissipation bounds the amplification of transition rates far from equilibrium. *Proc. Natl. Acad. Sci. U.S.A.* **118** (2021).
8. A. Das, B. Kuznets-Speck, D. T. Limmer, Direct evaluation of rare events in active matter from variational path sampling. *Phys. Rev. Lett.* **128**, 028005 (2022).
9. S. Whitelam, Strong bonds and far-from-equilibrium conditions minimize errors in lattice-gas growth. *J. Chem. Phys.* **149**, 104902 (2018).
10. M. Nguyen, Y. Qiu, S. Vaikuntanathan, Organization and self-assembly away from equilibrium: Toward thermodynamic design principles. *Annu. Rev. Condens. Matter Phys.* **12** (2021).
11. P. Charbonneau, D. Reichman, Phase behavior and far-from-equilibrium gelation in charged attractive colloids. *Phys. Rev. E* **75**, 050401 (2007).
12. A. Chremos, K. Margaritis, A. Z. Panagiotopoulos, Ultra thin films of diblock copolymers under shear. *Soft Matter* **6**, 3588–3595 (2010).
13. J. Stenhammar, A. Tiribocchi, R. J. Allen, D. Marenduzzo, M. E. Cates, Continuum theory of phase separation kinetics for active Brownian particles. *Phys. Rev. Lett.* **111**, 145702 (2013).
14. Y. Wang, H. Xu, X. Zhang, Tuning the amphiphilicity of building blocks: Controlled self-assembly and disassembly for functional supramolecular materials. *Adv. Mater.* **21**, 2849–2864 (2009).
15. G. K. Atkin-Smith, I. K. Poon, Disassembly of the dying: Mechanisms and functions. *Trends Cell Biol.* **27**, 151–162 (2017).
16. B. A. Grzybowski, K. Fitzner, J. Paczesny, S. Granick, From dynamic self-assembly to networked chemical systems. *Chem. Soc. Rev.* **46**, 5647–5678 (2017).

17. A. Murugan, D. A. Huse, S. Leibler, Speed, dissipation, and error in kinetic proofreading. *Proc. Natl. Acad. Sci. U.S.A.* **109**, 12034–12039 (2012).
18. F. Knoch, T. Speck, Nonequilibrium Markov state modeling of the globule-stretch transition. *Phys. Rev. E* **95**, 012503 (2017).
19. A. Albaugh, T. R. Gingrich, Simulating a chemically fueled molecular motor with nonequilibrium molecular dynamics. *Nat. Commun.* **13**, 1–10 (2022).
20. U. Seifert, Stochastic thermodynamics, fluctuation theorems and molecular machines. *Rep. Prog. Phys.* **75**, 126001 (2012).
21. A. Das, D. T. Limmer, Variational design principles for nonequilibrium colloidal assembly. *J. Chem. Phys.* **154**, 014107 (2021).
22. A. Das, D. T. Limmer, Variational control forces for enhanced sampling of nonequilibrium molecular dynamics simulations. *J. Chem. Phys.* **151**, 244123 (2019).
23. M. F. Hagan, D. Chandler, Dynamic pathways for viral capsid assembly. *Biophys. J.* **91**, 42–54 (2006).
24. A. C. Newton, J. Groenewold, W. K. Kegel, P. G. Bolhuis, Rotational diffusion affects the dynamical self-assembly pathways of patchy particles. *Proc. Natl. Acad. Sci. U.S.A.* **112**, 15308–15313 (2015).
25. R. L. Jack, M. F. Hagan, D. Chandler, Fluctuation–dissipation ratios in the dynamics of self-assembly. *Phys. Rev. E* **76**, 021119 (2007).
26. C. P. Goodrich, E. M. King, S. S. Schoenholz, E. D. Cubuk, M. P. Brenner, Designing self-assembling kinetics with differentiable statistical physics models. *Proc. Natl. Acad. Sci. U.S.A.* **118**, e2024083118 (2021).
27. M. Z. Miskin, G. Khaira, J. J. de Pablo, H. M. Jaeger, Turning statistical physics models into materials design engines. *Proc. Natl. Acad. Sci. U.S.A.* **113**, 34–39 (2016).
28. J. D. Weeks, D. Chandler, H. C. Andersen, Role of repulsive forces in determining the equilibrium structure of simple liquids. *J. Chem. Phys.* **54**, 5237–5247 (1971).
29. W. B. Rogers, J. C. Crocker, Direct measurements of DNA-mediated colloidal interactions and their quantitative modeling. *Proc. Natl. Acad. Sci. U.S.A.* **108**, 15687–15692 (2011).
30. V. N. Manoharan, Colloidal matter: Packing, geometry, and entropy. *Science* **349**, 1253751 (2015).
31. G. Meng, N. Arkus, M. P. Brenner, V. N. Manoharan, The free-energy landscape of clusters of attractive hard spheres. *Science* **327**, 560–563 (2010).
32. Z. Zeravcic, V. N. Manoharan, M. P. Brenner, Size limits of self-assembled colloidal structures made using specific interactions. *Proc. Natl. Acad. Sci. U.S.A.* **111**, 15918–15923 (2014).
33. D. Chandler, Statistical mechanics of isomerization dynamics in liquids and the transition state approximation. *J. Chem. Phys.* **68**, 2959–2970 (1978).
34. L. Onsager, S. Machlup, Fluctuations and irreversible processes. *Phys. Rev.* **91**, 1505 (1953).
35. P. B. Warren, R. J. Allen, Malliavin weight sampling for computing sensitivity coefficients in Brownian dynamics simulations. *Phys. Rev. Lett.* **109**, 250601 (2012).
36. S. Hormoz, M. P. Brenner, Design principles for self-assembly with short-range interactions. *Proc. Natl. Acad. Sci. U.S.A.* **108**, 5193–5198 (2011).
37. Y. Dou *et al*., A review on self-assembly in microfluidic devices. *J. Micromech. Microeng.* **27**, 113002 (2017).
38. D. Richard, T. Speck, The role of shear in crystallization kinetics: From suppression to enhancement. *Sci. Rep.* **5**, 1–7 (2015).
39. C. W. Gardiner *et al*., *Handbook of Stochastic Methods* (Springer, Berlin, Germany, 1985), vol. 3.
40. S. Schneider *et al*., Shear-induced unfolding triggers adhesion of von Willebrand factor fibers. *Proc. Natl. Acad. Sci. U.S.A.* **104**, 7899–7903 (2007).
41. J. Vermant, M. J. Solomon, Flow-induced structure in colloidal suspensions. *J. Phys.: Condens. Matter* **17**, R187 (2005).
42. S. Toyabe, H. R. Jiang, T. Nakamura, Y. Murayama, M. Sano, Experimental test of a new equality: Measuring heat dissipation in an optically driven colloidal system. *Phys. Rev. E* **75**, 011122 (2007).
43. M. W. Wu, R. A. Register, P. M. Chaikin, Shear alignment of sphere-morphology block copolymer thin films with viscous fluid flow. *Phys. Rev. E* **74**, 040801 (2006).
44. A. Alexander-Katz, M. Schneider, S. Schneider, A. Wixforth, R. Netz, Shear-flow-induced unfolding of polymeric globules. *Phys. Rev. Lett.* **97**, 138101 (2006).
45. E. K. Hill, B. Krebs, D. G. Goodall, G. J. Howlett, D. E. Dunstan, Shear flow induces amyloid fibril formation. *Biomacromolecules* **7**, 10–13 (2006).
46. J. Liphardt, S. Dumont, S. B. Smith, I. Tinoco Jr, C. Bustamante, Equilibrium information from nonequilibrium measurements in an experimental test of Jarzynski's equality. *Science* **296**, 1832–1835 (2002).
47. Y. Zhuang, P. Charbonneau, Recent advances in the theory and simulation of model colloidal microphase formers. *J. Phys. Chem. B* **120**, 7775–7782 (2016).
48. M. F. Hagan, G. M. Grason, Equilibrium mechanisms of self-limiting assembly. *Rev. Mod. Phys.* **93**, 025008 (2021).
49. D. L. Caspar, A. Klug, "Physical principles in the construction of regular viruses" in *Cold Spring Harbor Symposia on Quantitative Biology* (Cold Spring Harbor Laboratory Press, 1962), vol. 27, pp. 1–24.
50. S. Tanaka *et al*., Atomic-level models of the bacterial carboxysome shell. *Science* **319**, 1083–1086 (2008).
51. E. M. Courchaine, A. Lu, K. M. Neugebauer, Droplet organelles? *EMBO J.* **35**, 1603–1612 (2016).
52. D. Zwicker, A. A. Hyman, F. Jülicher, Suppression of Ostwald ripening in active emulsions. *Phys. Rev. E* **92**, 012317 (2015).
53. J. Söding, D. Zwicker, S. Sohrabi-Jahromi, M. Boehning, J. Kirschbaum, Mechanisms for active regulation of biomolecular condensates. *Trends Cell Biol.* **30**, 4–14 (2020).
54. J. Kirschbaum, D. Zwicker, Controlling biomolecular condensates via chemical reactions. *J. R. Soc. Interface* **18**, 20210255 (2021).
55. C. A. Brackley *et al*., Ephemeral protein binding to DNA shapes stable nuclear bodies and chromatin domains. *Biophys. J.* **112**, 1085–1093 (2017).
56. S. Toxvaerd, J. C. Dyre, Communication: Shifted forces in molecular dynamics. *J. Chem. Phys.* **134**, 081102 (2011).
57. T. C. Michaels *et al*., Dynamics of oligomer populations formed during the aggregation of Alzheimer's aβ42 peptide. *Nat. Chem.* **12**, 445–451 (2020).
58. V. Sourjik, H. C. Berg, Functional interactions between receptors in bacterial chemotaxis. *Nature* **428**, 437–441 (2004).
59. S. Whitelam, R. Schulman, L. Hedges, Self-assembly of multicomponent structures in and out of equilibrium. *Phys. Rev. Lett.* **109**, 265506 (2012).
60. A. Das, D. Limmer, avishek-das1/noneq-functional-design: Nonequilibrium design strategies for functional colloidal assemblies. Zenodo. https://zenodo.org/record/8031998. Deposited 13 June 2023.